International Journal of Hydrogen Energy 62 (2024) 375–388

Contents lists available at ScienceDirect

International Journal of Hydrogen Energy

journal homepage: www.elsevier.com/locate/he

Flow rate control in a plug-flow reactor for liquid organic hydrogen carriers dehydrogenation

Marco Gambini, Federica Guarnaccia, Michele Manno *, Michela Vellini

University of Rome Tor Vergata, Via del Politecnico, 1, Rome, 00133, Italy

ARTICLE INFO

Keywords:
Hydrogen storage
Plug flow reactor
LOHC
NEC
Control strategies
Energy–power relation

ABSTRACT

Liquid organic hydrogen carriers can store hydrogen for later release through dehydrogenation reactions. The kinetic rate depends on the temperature, pressure, and hydrogen concentration itself, so it varies throughout the discharge. As such, control systems are needed to meet the end-user power demand. An innovative plug flow reactor coupled with two vessels is introduced and accurately sized. Multiple strategies are implemented in a Matlab/Simulink model to test the efficacy of control methods based on pressure, temperature, and mass flow rate. The results obtained with the simulations highlight a dramatic drop in performance (utilisation factor lower than 80 %) associated with relatively high power demands (higher than 70 % in the case of temperature control), whereas low demands are met with satisfactory degrees of utilisation under both pressure and temperature control. Control over the mass flow rate of external fluid leads to lackluster results and should only be chosen as an auxiliary controlled variable. Lastly, Ragone diagrams for pressure and temperature control are presented and used to identify the optimal system sizing range: effective discharge duration should be in the range 10–40 h with pressure control or 5–40 h with temperature control to achieve a utilisation factor of at least 80 %.

1. Introduction

Hydrogen energy could play a significant role in the future due to its versatility, as it could both allow decarbonisation in sectors difficult to absorb (such as steel [1], copper [2] and cement production [3]), and support the integration of variable renewables into the electricity grid [4]. Forecasts show an increase in hydrogen uptake in the energy mix from 0.05 % possibly reached in 2030, to about 5.00 % by 2050, while accounting for even double these percentages in some countries [5]. However, there are many open challenges to address that require enabling measures to accelerate the growth of the green energy market [6–8]. Some of these issues depend on the technology readiness level of associated systems, such as electrolysers and fuel cells [9,10], and alternative production methods result in different levels of sustainability, cost, and energy efficiency [11]. In fact, emerging techniques for green hydrogen production arise from many industrial sectors [12]. Regulatory frameworks and standardisation will be required to help promote the diffusion of hydrogen technologies [13,14], and hydrogen integration will require evaluations of techno-economic effectiveness [15,16]. A key element in the development of innovative hydrogen-reliant energy systems is hydrogen storage [17–19], although it introduces additional issues such as toxicity and low energy density [20]. The more traditional routes, compressed [21] and liquid hydrogen [22], both have their own limits and disadvantages, and alternative routes are necessary.

Liquid organic hydrogen carriers (LOHCs) can serve as a material storage medium [23]. Storage is provided by the reversible saturation of double carbon–carbon bonds, and dehydrogenation takes place through progressive endothermic reactions. LOHCs are arguably more competitive than traditional hydrogen storage solutions for long-distance and large-scale applications [24].

To refer to the stored hydrogen content, a dimensionless parameter is commonly introduced as the degree of hydrogenation (DoH) defined as Eq. (1) [25]:

$$\mathrm{DoH} = n_{\mathrm{H_2}} / n_{\mathrm{H_2,max}} \tag{1}$$

which enables a simplified schematisation of the effective reaction taking place: instead of a multi-step reaction, only the fully loaded, and unloaded compounds are usually accounted for [26].

Fig. 1 portrays LOHC's integration with the electricity bus. First, hydrogen has to be produced, ideally as green hydrogen from excess

* Corresponding author.
E-mail addresses: gambini@ing.uniroma2.it (M. Gambini), federica.guarnaccia@students.uniroma2.eu (F. Guarnaccia), michele.manno@uniroma2.it (M. Manno), vellini@ing.uniroma2.it (M. Vellini).

https://doi.org/10.1016/j.ijhydene.2024.03.082
Received 29 November 2023; Received in revised form 6 February 2024; Accepted 6 March 2024
Available online 12 March 2024

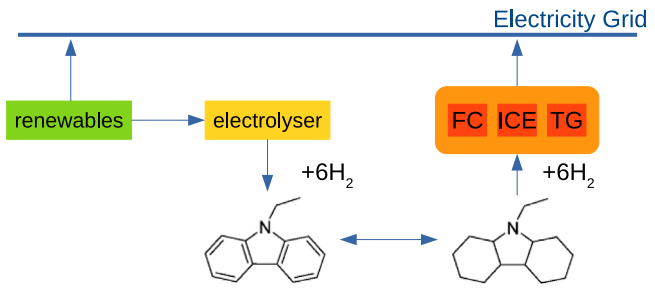

Fig. 1. Schematic view over the possible introduction of LOHC systems in more complex energy systems.

energy of a renewable source. After going through exothermic saturation of the double carbon–carbon bonds, the saturated LOHC is stored until needed. While consumption in situ is an option, LOHC systems could also be transported over long-distances.

The transport of hydrogen from its production plant to a terminal LOHC refuelling station has been found to be cheaper than compressed, liquefied, or pipeline hydrogen for long-distance, large-volume (more than 20 000 kg/d) hydrogen demands [27], and can reach the lowest levelised costs when considering the entire supply chain [28]. Consequently, projects are being developed for large volumes of hydrogen shipping overseas [29].

To satisfy the energy demand, LOHCs are dehydrogenated; reaction kinetics requires high temperature, with heat being sunk from the system, and low pressure levels [30].

Multiple carriers have been proposed over the years, and comparisons are still being made with respect to their thermophysical and kinetic properties, toxicity, costs, etc. [31,32]. As hydrogen can only be released providing heat at high temperatures, waste heat recovery [33] and system integration strategies are key to achieving profitability [34,35]. Techno-economic analyses point out that dehydrogenation heat demand and loading costs must be addressed, and heterocyclic compounds could lower such costs [36,37]. Among these compounds, a prominent carrier is N-ethyl-carbazole [30,38,39]. Hetero-atoms containing carriers are best suited for on-board dehydrogenation, however their implementation still has to account for some notable drawbacks such as high synthesis costs of the raw materials, and a relatively high melting point which could make long-distance applications more complex [32,40].

The high temperature favours both the equilibrium composition of dehydrogenation and its kinetics, and the low pressure leads to similar results, as a greater number of moles of gas are present on the product side. However, the uncontrolled kinetic rate is also widely variable, as dehydrogenation in most carriers follows a second-order reaction trend [41], and as such it slows down quickly as the degree of hydrogenation decreases [30,42]. Unless a control strategy is in place, the system is thus unable to consistently meet the end-user demand.

Although control strategies to meet a well-defined power demand have been extensively studied for metal hydrides [43–45], studies on LOHC systems are mainly focused on the end user [26,42], with little to no focus on the control system. Control strategies are better highlighted by Geiling et al. where a PI controller is used to meet the target power demand through pressure control [46]. However, the authors focus on the dynamic fuel cell operation and not on the controllability itself. Similarly, the effects of changes in pressure and temperature on the release rate have been compared in terms of how quickly the reactor adapts to the new setup [47]. Common designs are plug flow reactors (PFRs) partially filled with a catalytic bed, yet providing enough space for hydrogen discharge [42,48,49] but with cumbersome layouts. Different designs have also been proposed [50], but are yet to be used in simulations of complex energy systems.

This paper provides an innovative approach to LOHC-based systems, focusing on LOHC controllability and not on their integration in complex energy systems. Alternative control strategies are studied and compared for different power demands and implemented in an innovative reactor design with a compact layout that allows intermittent operation. The results obtained are therefore used both to graph Ragone plots [51–53] so that the power demand levels are associated with the maximum energy that can be released at any given rate, and also to provide sizing guidelines to grant adequate energy densities.

As such, controllability is defined in terms of the capability of the system to meet the target demand over an extended period. Rather than accounting for time-spans, which would be affected by the power level required (i.e. for a given size in terms of energy content, greater power demand are intrinsically related to a lower time duration), performances are evaluated looking at the lower hydrogenation level at which the system can still meet the demand.

2. Methods

A simple closed-loop tubular PFR equipped with two vessels, described by the simplified layout represented in Fig. 2, is first simulated and optimised in Matlab, and then the model is replicated in Simulink with an appropriate geometric configuration as input. Multiple control strategies are implemented and tested for an increasingly high constant power demand. The released hydrogen flow rate is controlled by means of PI controllers acting alternatively on three different controlled variables: reactor pressure (Fig. 2(a)), Heat Transfer Fluid (HTF) inlet temperature, or HTFmass flow rate (Fig. 2(b)). Power demand values are defined using the maximum hydrogen discharge rate as reference (defined in Section 2.2.1), so that the final results are size-independent. N-Ethyl-Carbazole (NEC) is selected as the carrier, and its kinetic parameters are taken from a previous work [30]. Thermophysical properties are modelled with group contribution methods for organic liquids and mixtures, based on 12H-NEC and 0H-NEC molecules [54].

As LOHC dehydrogenation can be modelled as follows [30]:

$$\frac{\partial \mathrm{DoH}}{\partial t} = k_{cat} \cdot f(T) \cdot g(p) \cdot z(\mathrm{DoH}) \tag{2}$$

with Arrhenius-like temperature dependence, an exponential pressure dependence, and a DoH dependence in the form of a power law, different carriers (and catalysts) while modelled similarly require different coefficient values. As such, the proposed model and analysis can be applied to any carrier, however numerical results may change [26,30]. Overall, adapting the model to a new carrier would only require changing the kinetic law coefficients, and the reaction heat value.

2.1. Reactor

Different reactor designs have been examined. The proposed layout is described in Section 2.1.1: it was selected because of its compactness and intrinsic potential for continuous and discontinuous operation. The equations required to model the reactor and its vessels are shown in Section 2.1.2, and grid convergence is tested in Section 2.1.4. Lastly, the simulation parameters are summarised in Section 2.1.3.

2.1.1. Description

The proposed design consists of a tubular PFR half-filled with a catalytic bed [42] through which the LOHC is released from one of the adjacent vessels, while the other (passive) is filled by the reactor outlet, and it is assumed that hydrogen is collected above the reactor itself without hindering the reaction. When the feeding (active) vessel is finally empty, the passive vessel switches to the active mode, and vice versa. The flow is reversed in the reactor as relatively high DoH LOHC is fed from the opposite side.

This configuration allows for a wider design freedom: the energy content of the system can easily be correlated to the LOHC volume, however, reactor diameter and length are not uniquely defined. For a

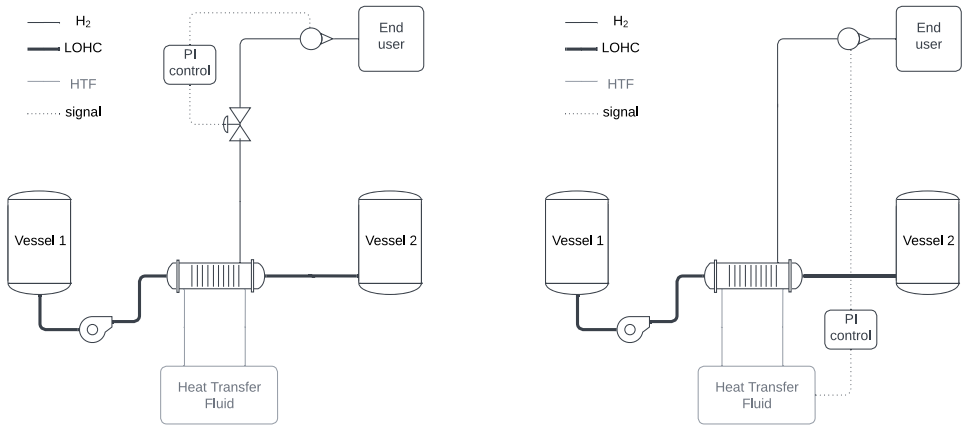

(a) Pressure control. (b) HTF (inlet temperature or flow rate) control.

Fig. 2. Simplified layout of the hydrogen storage system with flow rate control.

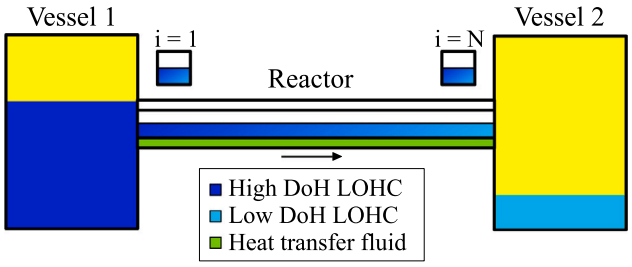

Fig. 3. Reactor's design schematic representation. Vessel 1 and 2 alternates operation mode, switch from active to passive and vice versa at each new turn.

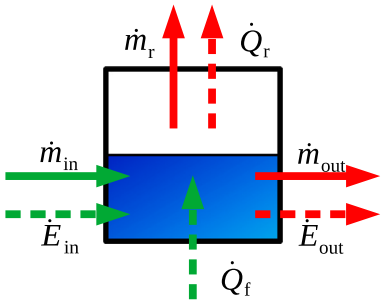

Fig. 4. Generic integration element for the tubular reactor. The flow directions are chosen with respect to odd turns.

given overall volume (energy content) and a fixed reactor length, the greater the hydrogen content of the vessels, the smaller the instantaneous power release as a reduced mass flow rate crosses the reactor. A shift towards lighter vessels increases the volume of the tubular reactor, and for a given length implies a higher power release. However, in this design, it is not necessary to set the length of the reactor: assuming isothermal kinetics, the residence time in the reactor can be quantified for given values of final (DoH_f) and initial (DoH_0) degree of hydrogenation. This requirement can be applied to any combination of the LOHC velocity v_L, the reactor length L, and the turn number n that satisfies Eq. (3).

$$\tau_{reaction} = nL/v_L \tag{3}$$

The multitude of parameters available to achieve the desired reactor performance make this layout a promising alternative to more traditional designs. The layout used for this paper was chosen so that high heat transfer efficiency, low pumping power loss, and compact volumes are all achieved. Design parameters could be optimised to better tune reactor performance; however, this step was deemed unnecessary for the purpose of this article.

A simplified design is proposed in Fig. 3, with vessel 1 acting as the active vessel in the picture. Simulations were performed starting with a totally empty passive vessel. Both vessels are kept at the design temperature during the discharge process; in fact, only a small percentage of additional heat must be supplied compared to the much higher energy content required to keep the reactor near the desired operating point.

2.1.2. Mass and energy balance

Mass and energy balance have been written and implemented for the reactor and the active and passive vessel. More specifically:

- Active vessel: Eq. (4) represents the energy balance, with the first member representing the variation in internal energy (with respect to the specific heat capacity of the LOHC mass content and its derivative, and the LOHC temperature and its derivative), while the right side features the energy flux related to the outlet flow ($\dot{m}_{v,a}$) and the heat to supply to keep a constant temperature over time, with respect to the enthalpy and kinetic energy content.

$$c_l m_{v,a} \frac{dT_{v,a}}{dt} + c_l T_{v,a} \frac{dm_{v,a}}{dt} = \dot{Q}_{v,a} - \dot{m}_{v,a}\left(\Delta h + \frac{v_{v,a}^2}{2}\right) \tag{4}$$

Eq. (5) then accounts for the mass balance, with the outlet mass flow rate $\dot{m}_{v,a}$ defined by Eq. (6) having set the desired discharge time (t_v) for the vessel.

$$\frac{dm_{v,a}}{dt} = -\dot{m}_{v,a} \tag{5}$$

$$\dot{m}_{v,a} = m_{v,\mathrm{LOHC}^-}/t_v \tag{6}$$

It should be noted that t_v is constant throughout discharge, since its definition is based on dehydrogenated LOHC ($LOHC^-$) only, assuming that the LOHC vapours are negligible. Lastly, Eq. (7) accounts for the variation of the hydrogen content in the active vessel over time; as no reaction takes place inside the vessel, $DoH_{v,a}$ is constant during discharge for a given turn.

$$\frac{dm_{v,a}^{H_2}}{dt} = -w_{\%}\mathrm{DoH}_{v,a}\dot{m}_{v,a} \tag{7}$$

- Passive vessel: similar to the active vessel model, Eq. (8) accounts for the energy balance, but this time the mass flow rate enters the

vessel. Eq. (9) represents the mass balance with the index i, which refers to the discretisation of the reactor, defined as $\bar{i} = 1$ during odd turns when a scheme like the one in Fig. 3 is deployed as initial configuration, and $\bar{i} = \mathrm{N}$ during even turns.

$$c_l m_{v,p} \frac{\mathrm{d}T_{v,p}}{\mathrm{d}t} + c_l T_{v,p} \frac{\mathrm{d}m_{v,p}}{\mathrm{d}t} = \dot{Q}_{v,p} + \dot{m}_{\bar{i}} \left(\Delta h + \frac{v^2_{out,\bar{i}}}{2} \right) \tag{8}$$

$$\frac{\mathrm{d}m_{v,p}}{\mathrm{d}t} = \dot{m}_{\bar{i}} \tag{9}$$

A more compact and useful definition of $\bar{i}$ is Eq. (10), with coefficients c_1 and c_2 defined in the next paragraph dedicated to the reactor.

$$\bar{i} = c_1 \cdot N + c_2 \cdot 1 \tag{10}$$

Eq. (11) accounts for the hydrogen mass balance, while this time the vessel DoH has to be evaluated over time as Eq. (12) since transient behaviour is expected at the start of every new turn, and as such $\mathrm{DoH}_{\bar{i}}$ is not constant throughout the whole turn.

$$\frac{\mathrm{d}m^{\mathrm{H_2}}_{v,p}}{\mathrm{d}t} = -w_{\%} \mathrm{DoH}_{\bar{i}} \dot{m}_{\bar{i}} \tag{11}$$

$$\mathrm{DoH}_{v,p} = \frac{m^{\mathrm{H_2}}_{v,p}}{m_{v,p} w_{\%}} \tag{12}$$

- Reactor: having divided the tubular reactor into different control volumes, as shown in Fig. 4, Eq. (13) represents the energy balance in each reactor control volume, where the terms on the right side represent the external heat rate provided through HTF (Eq. (14)), the reaction heat rate (Eq. (15)), and the net energy flux (Eq. (16)).

$$c^i_L m^i \frac{\mathrm{d}T^i}{\mathrm{d}t} + c^i_L T^i \left(\frac{\mathrm{d}m^i}{\mathrm{d}t} - \frac{\mathrm{d}m^i_r}{\mathrm{d}t} \right) = \dot{Q}^i_f + \dot{Q}^i_r + \dot{E}^i_m \tag{13}$$

$$\dot{Q}^i_f = \dot{m}_f c_f \varepsilon (T_f - T^i) \tag{14}$$

$$\dot{Q}^i_r = \dot{m}^i_{\mathrm{H_2},r} (-\Delta H_r + (\Delta u^i_{\mathrm{H_2}} - \Delta h^i_{\mathrm{H_2}})) \tag{15}$$

$$\dot{E}^i_m = \dot{m}^i_{in} \left(\Delta h^{i-1} + \frac{v^{i-1,2}}{2} \right) - \dot{m}^i_{out} \left(\Delta h^i + \frac{v^{i,2}}{2} \right) \tag{16}$$

Eq. (14) requires the definition of the heat exchanger effectiveness (ε), calculated using Eqs. (17)–(18) based on the NTU approach where the latter is evaluated with respect to the heat exchange surface times the overall heat transfer coefficient by the HTF heat capacity, and is then used to evaluate the heat transfer effectiveness.

$$\varepsilon = 1 - \exp(-\mathrm{NTU}) \tag{17}$$

$$\mathrm{NTU} = \frac{U A_{hex}}{\dot{m}_f c_f} \tag{18}$$

The definition of the overall heat transfer coefficient U, Eq. (19), depends on the thermal conductivity λ of the reactor wall and the convective heat transfer coefficients of LOHC and HTF (α_L, α_f).

$$U = \left(\frac{1}{\alpha_f} + \frac{D_2 \log(D_2/D_1)}{2\lambda} + \frac{D_2}{D_1} \frac{1}{\alpha_L} \right)^{-1} \tag{19}$$

Dixon and Cresswell relation [49] are chosen to evaluate the carrier Nusselt number Nu_L through the catalytic bed, Eq. (20), while the Gnielinski and Blasius equations provide Nu_f for the HTF in Eqs. (21)–(22).

$$\mathrm{Nu}_L = 0.523 \left(1 - \frac{d_p}{D_{hyd,L}} \right) \mathrm{Pr}_L^{0.33} \mathrm{Re}_L^{0.738} \tag{20}$$

$$f = 0.3164 \mathrm{Re}_f^{-0.25} \tag{21}$$

$$\mathrm{Nu}_f = \frac{f}{8} (\mathrm{Re}_f - 1 \times 10^3) \frac{\mathrm{Pr}_f}{1 + 12.7 \sqrt{\frac{f}{8}} \left(\mathrm{Pr}_f^{2/3} - 1 \right)} \tag{22}$$

The reaction heat rate, Eq. (15), depends on the amount of hydrogen released, which can be expressed as in Eq. (23), having assumed a constant pressure level throughout the length of the reactor, and having separated the actual kinetic term (on the right) depending on the reaction by a scale factor, given by the LOHC mass multiplied by the gravimetric energy density of the fully hydrogenated LOHC.

$$\dot{m}^i_r = (w_{\%} m^i) \cdot \left[k_0 \exp \left(-bp - \frac{E_a}{R_u T^i} \right) \mathrm{DoH}^{i2} \right] \tag{23}$$

Lastly, Eq. (16) features the contribution of the mass flow rate from the inlet and outlet due to its enthalpy and kinetic energy content. The velocity is estimated with Eq. (24)–(25), depending on the filled cross section and the mass flow rate leaving the element ($\dot{m}^i_{out}$) evaluated as in Eq. (26).

$$\Omega^i = m^i / \left(\rho^i_L d z \right) \tag{24}$$

$$v^i = \dot{m}^i_{out} / \left(\rho^i_L \Omega^i \right) \tag{25}$$

$$\dot{m}^i_{out}(t) = \dot{m}^i_{in}(t-1) - \dot{m}^i_r \tag{26}$$

Finally, the inlet mass flow rate ($\dot{m}^i_{in}$) corresponds to either the vessel outflow, or the adjoining element outlet mass flow rate. To maintain a consistent grid element numbering throughout both operating modes (Section 2.1.1), the coefficients c_1 and c_2 are introduced in Eq. (27) and defined as follows:

$$c_1 = \mod [j_{turn}, 2]$$

$$c_2 = \mod [j_{turn} + 1, 2]$$

so that during odd turns c_1 is unitary and c_2 is null, and vice versa during even turns.

$$\dot{m}_{in} = \left[\dot{m}_{v,a}, \dot{m}_{out}(1 : N-1) \right] \cdot c_1 + c_2 \cdot \left[\dot{m}_{out}(2 : N), \dot{m}_{v,a} \right] \tag{27}$$

Furthermore, the Colebrook equation, Eq. (28), is used to provide an estimate of the friction factor (f) required to assess the pressure drop, Eq. (29), and then the dissipated power Eq. (30).

$$\frac{1}{\sqrt{f}} = -2 \log \left(\frac{\epsilon_{tube}}{3.7 D_{hyd}} + \frac{2.51}{\mathrm{Re}\sqrt{f}} \right) \tag{28}$$

$$\Delta p_{loss} = f \frac{L}{D_{hyd}} \frac{\rho v^2}{2} \tag{29}$$

$$P_{pump} = \Delta p_{loss} \dot{m} / \rho \tag{30}$$

2.1.3. Design parameters

The LOHC mass inside the storage system has been calculated with the assumption of feeding a solid oxide fuel cell, operating with a 45 % average efficiency (based on the higher heating value of hydrogen), producing 50 kWh of net electric energy: the required hydrogen mass is $m_{\mathrm{H_2}} = 2.821\,\mathrm{kg}$, which is made available by a NEC mass m_L resulting from Eq. (31), taking into account its theoretical gravimetric density, $w = 5.84\%$, and the minimum and maximum values of DoH, which are listed in Table 1 together with the other parameters used to design the storage system. *Dowtherm Q* has been selected as the HTF, and its properties are taken from *CoolProp* [55].

$$m_L = \frac{m_{\mathrm{H_2}}}{w \left(\mathrm{DoH}_{\max} - \mathrm{DoH}_{\min} \right)} = 64.40\,\mathrm{kg} \tag{31}$$

It should be noted that the total hydrogen mass $m_{\mathrm{H_2},tot}$ that is potentially available for discharge is greater than $m_{\mathrm{H_2}}$, which is limited by the lower and upper limits considered on the degree of hydrogenation. If such constraints are removed, and a theoretical discharge from DoH = 1 to DoH = 0 is considered, the total mass of hydrogen available becomes:

$$m_{\mathrm{H_2},tot} = w m_L = \frac{m_{\mathrm{H_2}}}{\mathrm{DoH}_{\max} - \mathrm{DoH}_{\min}}. \tag{32}$$

Table 1
Design, kinetic, and thermodynamic parameters used for the simulations.

Parameter	Value	Unit	Ref.
Available H_2 mass (m_{H_2})	2.821	kg	–
LOHC mass (m_L)	64.40	kg	–
Design temperature (T_{des})	473.15	K	[30]
Design pressure (p_{des})	1.50	bar	[56]
Initial hydrogen content (DoH_{max})	0.95	–	[42]
Final hydrogen content (DoH_{min})	0.20	–	[42]
NEC properties			
Gravimetric density (w)	5.84	%	–
Activation energy (E_a)	121×10^3	kJ/mol	[30]
Pressure coefficient (b)	1.397	1/bar	[30]
Frequency factor (k_0)	2.609×10^{12}	1/min	[30]
Reaction enthalpy (ΔH_r)	50.6	kJ/mol_{H_2}	[40]
HTF properties (reference values)			
Inlet temperature (T_f)	473.15	K	–
Velocity (v_f)	0.58	m/s	–
Mass flow rate ratio (f_x)	1.00	–	–
Miscellaneous design properties			
LOHC velocity (v_L)	0.10	m/s	–
Vessel emptying time (t_v)	240	s	–
Reactor mass ratio (f_r)	0.20	–	–

With the parameters listed in Table 1, the total hydrogen mass $m_{H_2,tot}$ is 3.761 kg.

The parameters f_r, defined by Eq. (33), t_v, defined by Eq. (6), f_x, defined by Eq. (34), v_L and v_f are chosen to satisfy effectiveness, sizing, and power constraints expressed in the following.

$$f_r = m_{reactor}(t_0)/m_{tot}(t_0) \tag{33}$$

$$f_x = \dot{m}_f/\dot{m}_{\mathrm{LOHC}^-} \tag{34}$$

These parameters are respectively associated to:

- f_r is the ratio of the reactor LOHC content to the system overall LOHC content ratio, so that higher values lead to a greater amount of LOHC in the reactor at any given time, thus making the scale factor in Eq. (23) greater, and the released mass flow rate higher;
- t_v is the time required to empty the vessel, which is proportional to the LOHC inlet speed: the faster it is for a given length, the lower the residence time so that limited dehydrogenation takes place;
- f_x is the ratio between the inlet HTF and LOHC mass flow rate: increasing this value leads to a higher heat capacity and can reduce temperature drop across the reactor;
- v_L and v_f are the LOHC and HTF velocity: an increase in any of these variables leads to higher heat transfer coefficients, with v_L factoring in the residence time, affecting how much the carrier is dehydrogenated for a given turn.

More specifically, the system parameters were chosen so that the pump power required to overcome the pressure losses, Eq. (30), is lower than a threshold defined as the 1.00 % of the minimum net power supplied by the reactor, Eq. (35).

$$P_{pump,\max} = 1\% \times f_r \cdot (w_{\%} m_{\mathrm{LOHC}^-}) \cdot \left[k_0 \exp\left(-bp_{des} - \frac{E_a}{R_u T_{des}}\right) \mathrm{DoH}_{\min}^2\right] \tag{35}$$

With this constraint in mind, design parameters were selected to both provide high heat transfer effectiveness, no lower than 95.0%, and to lead to a compact enough design.

2.1.4. Convergence

Simulations were performed for an increasing number of grid elements until convergence. Fig. 5 shows trends for both the required operation time τ, Eq. (36), and the relative error derived assuming $n_z = 200$ as reference, Eq. (37). The system converges with about 160–200 elements. The simulated setup had a f_v factor of 0.20 that led to such a high τ. Repeated simulations for different design parameters returned the same results; as such, n_z was set to 180.

$$\tau = t, \text{ such that: } \mathrm{DoH}(t) = 0.2 \tag{36}$$

$$\text{rel. err.}(n_z) = \frac{|\tau^{200} - \tau^{n_z}|}{\tau^{200}} \tag{37}$$

2.2. Control system

A control system has been implemented to control the hydrogen mass flow rate to a desired target value $\dot{m}_t$, defined in Section 2.2.1: then different scenarios of power demands are tested with three alternative control strategies, defined in Section 2.2.2. It should be noted that the mass flow rate and power demands (meaning the power generated by the end user of the hydrogen flow rate) are strictly correlated through Eq. (38), where P_t indicates the target power and η the end-user efficiency, and as such these terms are used interchangeably in this paper.

$$P_t = \dot{m}_t \mathrm{HHV} \eta \tag{38}$$

Similarly, the HTF mass flow rate is directly related to velocity, as shown by Eq. (39) where Ω_f denotes the cross section available to the HTF; so, the mass flow rate and velocity control are used in the following as synonyms, although velocity control has a secondary effect as explained in Section 2.2.2.

$$\dot{m}_f = \rho_f \Omega_f v_f \tag{39}$$

A simple PI controller has been chosen, as only constant demands are being tested and controllability performances are not affected by the controller but only by the physical constraints over the controlled variables, and the kinetic law itself.

Studying more complex solutions, multiple variables could be controlled at once, however this article is meant as a general sizing guide. While some control strategies could be intrinsically related (mainly mass flow rate and temperature control), the end-user could or could not be able to meet the specifications (for instance, temperature control could be limited by the upper temperature bound). As such, only single variable controls have been modelled: if more complex solutions are available, controllability is either extended, controlled variables are put under a reduced strain, or both. An exact quantification of such results requires the definition of an end-user type, and is thus beyond the scope of this article. Therefore, each control strategy has been tested separately, while setting the others to a constant value as indicated by Table 1.

2.2.1. Target definition

Instead of a quantile-based approach [39], to provide a more intuitive reference, the discharge targets are defined with respect to the maximum possible dehydrogenation rate, leading to a maximum flow rate $\dot{m}_{H_2,\max}$ defined by Eq. (40) that occurs when the system is fully charged ($\mathrm{DoH} = \mathrm{DoH}_{\max}$), the temperature is the design temperature $T = T_{des}$ and with the minimum value of the back pressure.

$$\dot{m}_{H_2,\max} = f_r(w_{\%} m_{\mathrm{LOHC}^-}) \left[k_0 \exp\left(-\left(bp_{\min} + \frac{E_a}{R_u T_{des}}\right)\right) \mathrm{DoH}_{\max}^n\right] \tag{40}$$

For the input parameters shown in Table 1, this value is $\dot{m}_{H_2,\max} = 0.19$ g/s. Consequently, the target flow rates are rewritten with respect to the maximum mass flow rate as in Eq. (41).

$$\dot{m}_t = f_t \dot{m}_{H_2,\max} \tag{41}$$

To lead a size-independent analysis, data are than presented in terms of the target scale factor (f_t), with a maximum value of $f_t = 1$ when $\dot{m}_t$ coincides with $\dot{m}_{H_2,\max}$. Theoretically, the system should be able

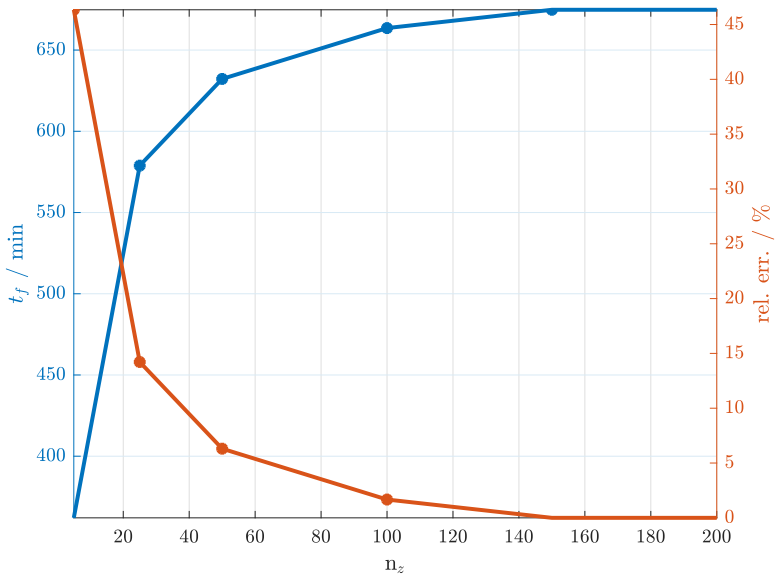

Fig. 5. Operation time for a 0.95–0.20 DoH discharge and its relative error.

to meet this scenario requirement only for an infinitesimally small period; however, range variability for each control variable can extend controllability over time.

Real applications could require some degree of load modulation; however, LOHC discharge capability is only related to DoH, temperature, and pressure levels for a given system. As such, if a non-constant demand has to be met, the bottleneck is not given by the LOHC, but by the end-user itself (turbines, fuel cells, and so on). A solid oxide application undergoing load reduction from 100%–50% has been modelled and it returned good performances [42]. However, for sizing applications, different loads do not introduce any significant change, see Section 3.3.

2.2.2. Control strategies

The selected control variables are:

- Pressure (p): it has a direct influence over the reaction rate and the released rate $\dot{m}_r$ as seen in Eq. (23). The higher the pressure, the slower the release, whereas low pressure favours dehydrogenation according to experimental data [57] and the Le Chatelier principle.
- HTF inlet temperature (T_f): the released mass flow rate $\dot{m}_r$ changes according to, again, Eq. (23); however, an indirect influence is introduced since the actual control variable is the HTF temperature, so the LOHC temperature changes due to Eqs. (13)–(14). The higher the temperature, the faster the reaction; however, lower temperature levels might also hinder the release acting on the equilibrium concentrations of the endothermic reaction.
- HTF velocity (v_f): similarly to T_f, v_f indirectly influences $\dot{m}_r$ through Eqs. (13)–(15). Unless a T_f lower than the carrier temperature is set, higher values favour a higher T^i and, consequently, faster release. Although the primary effect of v_f is on the mass flow rate through Eq. (39), and therefore the heat capacity in Eq. (14), a secondary effect is introduced in ε. However, unless low values of v_f are required, which reduce h_f and result in less effective heat transfer, this effect is mostly negligible, as an already high heat transfer effectiveness is expected.

Limiting upper and lower bounds for each variable range were selected as follows.

- Pressure: pressure inside the reactor must not drop lower than 1.0 bar to avoid additional measures to work below the environment pressure level; on the other hand, p cannot be higher than 5.0 bar above which different storage systems might be better suited.
- Temperature: the lower bound is set to the thermodynamic reference temperature of 298.15 K; conversely, the thermal stability of the carrier itself imposes a maximum acceptable temperature of 500.15 K [58].
- Velocity: a minimum value of $v_f = 0.0\,\mathrm{m/s}$ was chosen to simulate the lack of HTF mass flow rate, while the upper threshold is set to 1.25 m/s, according to the optimisation constraint on the maximum pumping power required, Eqs. (35)–(30).

Such limits influence the performance of each control system and could be subject to further discussion. This is especially true with respect to the temperature upper bound, as the availability of high-temperature sources is already the greatest weakness of LOHC systems, and the issue of thermal stability is still mostly neglected in many studies. Regardless of their exact value, the proposed ranges of variability are representative of the actual realistic control range for each variable.

3. Results and discussion

The layout proposed in Section 2.1 has been first simulated without the control system, and the final results are presented in Section 3.1. The controllability performances are then tested with a *Matlab/Simulink* model, having provided custom blocks to account for the kinetics and thermodynamics equations that describe both the reactor and the two vessels; the results are discussed in Section 3.2. The switch between active and passive operation mode for each vessel is implemented in *Stateflow*, based on the time instant when the active vessel is completely empty (every t_v). Lastly, the Ragone diagrams are presented in Section 3.3.

3.1. Uncontrolled system

In this section, the dynamic response of the uncontrolled system is discussed with reference to the total DoH of the storage system, which is defined in Eq. (42), and compared to the DoH of the two vessels.

$$\mathrm{DoH}_{tot}(t) = \frac{\sum_{i=1}^{N} m_i^{\mathrm{H_2}}(t) + \sum_{j=1}^{2} m_{v,j}^{\mathrm{H_2}}(t)}{m_{LOHC^-,tot}\, w_{\%}} \tag{42}$$

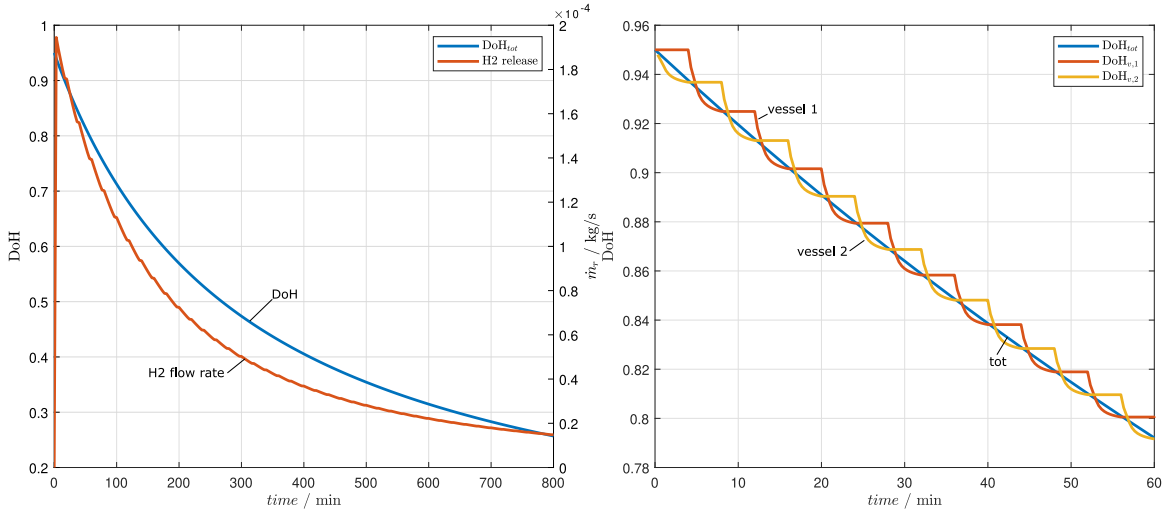

Fig. 6. Hydrogenation degree of the two vessels and the whole system over time, zoomed to better highlight how the system works on the right, and overall DoH and release trends on the left.

The results for the uncontrolled system are thus presented in Fig. 6 in terms of DoH_{tot} and each vessel's DoH. Design parameters have been chosen so that the whole system, while displaying different properties throughout its components and length, has similar DoH in the reactor and vessels alike. As a matter of fact, this is a consequence of the many turns needed to fully discharge the LOHC, and the small reactor length. As such, temporal variations are more marked than spatial variations, and to better understand the trends, a zoomed plot of the first 15 turns (60 min with t_v as in Table 1) is represented in Fig. 6.

At every time, one of the vessels acts as the active vessel, and, as a consequence, its DoH is constant until its mass content is null. Meanwhile, the other vessel is in passive mode: its mass content increases while the DoH is overall decreasing, and it goes through a first drop due to LOHC with higher reaction time entering it, and a consequent phase in which the DoH settles to some level as the transient effect of the operation mode switch wears off. The drop is actually due to the change in DoH associated with $\dot{m}_{v,a}$. Different values of t_v and reactor length would influence the balance between these two phases.

Meanwhile, total DoH has a smooth trend with the degree of hydrogenation in the active vessel $DoH_{v,a}$ serving as its upper limit. As discharge proceeds, DoH_{tot} becomes closer to the DoH in the passive vessel: LOHC content in the active vessel decreases, and an increasing amount of LOHC has already passed through the reactor for long periods of time. Just after the switch DoH_{tot} is actually slightly lower than both vessels. This is because the active vessel DoH is set to the DoH level just before the switch takes place, which is an averaged value (Eq. (12)) that accounts for the two alternating phases highlighted just before. As such, the DoH in the adjacent elements to this vessel is lower than the new $DoH_{v,a}$, which was kept high by the initially higher degrees of hydrogenation of the entering carrier. On the other hand, as it changes direction, the now passive vessel is fed by LOHC that had just been fluxed by it and has a high DoH level. It follows that the minimum DoH is not initially located at the adjacent elements of the passive reactor, so the overall DoH is lower than that of both vessels. The small length of the reactor keeps this phase very brief.

It should be noted that the discharge process described above requires the HTF to supply heat to the system, as indicated by Eq. (14); furthermore, in the configuration here proposed, each vessel is kept at a constant temperature T_{des}. Fig. 7 shows the composition of heat consumption by comparing the rate of heat transferred by the HTF ($\dot{Q}_f$) with additional heat demands, namely: LOHC preheating and vessel heating. These last two items are grouped into the "Others" category, which is then analysed in the inner chart.

While vessel heating refers to the heat provided to keep the temperature constant at T_{des} in both vessels during operation time, and is evaluated from Eqs. (4)–(8) having set the temperature derivatives equal to zero, and then summing and integrating over time both heat demands, LOHC preheating takes place before the beginning of the operation.

Fig. 7(a) differs from Fig. 7(b) due to different preheating initial conditions. In Fig. 7(a) less heat is required because the starting temperature is hypothesised to coincide with the hydrogenation reaction temperature. For NEC-based systems, this value is around 433 K [30]. As such, a 40 K ΔT is required. While this condition allows for a reduced heat consumption, it supposedly implies local use of the stored hydrogen.

On the other hand, ambient temperature was assumed as the starting condition for Fig. 7(b). The resulting preheating consumption is much higher but allows for long-distance dispatch of the stored energy content. However, it should be noted that actual consumption would likely be less than evaluated, since NEC is solid at ambient temperature [59], making transport at low temperature unlikely.

However, both cases are representative of the heat composition. This is mainly due to reactor heating and, more specifically, is mainly required to compensate for the reaction heat rate $\dot{Q}_r$, Eq. (15). The total heat consumption is around 72.4–75.6 MJ for the best- and worst-case scenarios, respectively, compared to about 71 MJ of the absorbed Q_r. These values are obtained for a 50 kWh system, so heat consumption accounts for more than 40 % of the energy content. Such figures reinforce the notion that a LOHC-based energy system can only be profitable when waste heat is used to reduce the heat demand. Furthermore, the reaction heat released during hydrogenation should be harvested to increase profitability; however, even if all this heat source were stored, it could only cover some of the LOHC preheating heat demand (assuming a starting temperature lower than the one in Fig. 7(a)), since heat would be released at a lower temperature than desired.

3.2. Controlled system

Controllability results are here presented for each controlled parameter, distinguishing between low ($f_t \leq 0.5$) and high ($f_t > 0.5$) power demand.

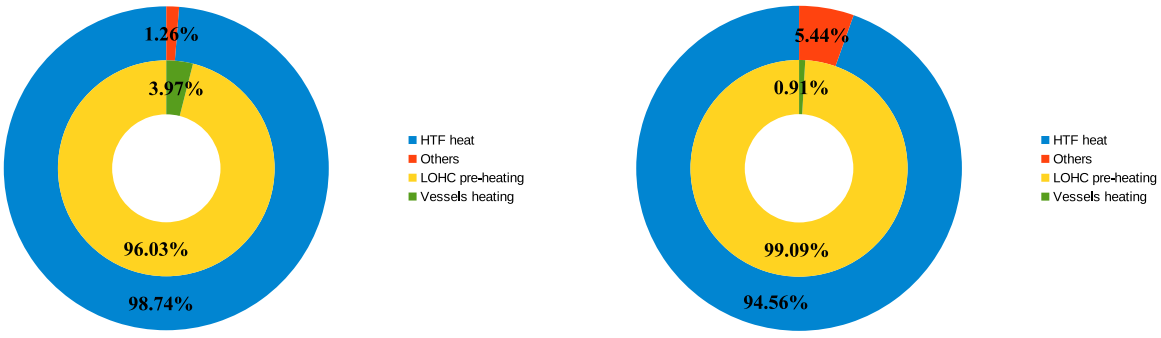

(a) Least expensive heat consumption.

(b) Most expensive heat consumption.

Fig. 7. Heat consumption composition distinguishing between reactor heating (HTF heat) and other sources (pre-heating, and vessels heating).

3.2.1. Pressure control

Fig. 8 shows the performance of a pressure control system for values of power fraction f_t in the range 0.10–0.50. Fig. 8(a) shows the change in DoH and the released mass fow rate over time: as long as the system can satisfy the constant power demand, DoH decreases linearly. Fig. 8(b) instead shows how the reactor pressure must change over time: the operating pressure must initially be increased to hinder the release process, as the high DoH allows for high dehydrogenation rates, as indicated by Eq. (23); then the operating pressure must decrease to compensate for the progressive reduction in DoH as hydrogen is released by the LOHC. Once the operating pressure is reduced to its minimum possible value, which depends on the back pressure of the end user (assumed here to be $p_{\min} = 1$ bar), the power demand cannot be sustained and the system is no longer controllable: it can further supply hydrogen only if the power demand is reduced. Therefore, a utilisation factor e can be introduced to measure the amount of hydrogen supplied to the end user against the available hydrogen stored in the system; the utilisation factor can also be interpreted as a dimensionless useful energy delivered by the system. The utilisation factor is defined in the following equation, where τ is the discharge duration, corresponding to the time instant when the system is no longer able to supply the required flow rate, and $m_{H_2,u}$ is the hydrogen mass that the system actually delivers to the end user for a given power demand:

$$e = \frac{\int_0^\tau \dot{m}_r \, dt}{m_{H_2}} = \frac{m_{H_2,u}}{m_{H_2}}. \tag{43}$$

The release curves in Fig. 8(a) highlight a good response of the system to the lowest demand ($f_t = 0.10$), as the system can maintain the required power demand over the whole DoH operating range. As demand increases, the operating time decreases due to physical constraints: since the energy content of the system is constant, the theoretical operating time is intrinsically lower; however, the lower bound over the controlled variable is not low enough to ensure the required power demand for low values of DoH, so that, for example, if the end user doubles the power demand, the operating time decreases by a higher factor. As a result, a fraction of hydrogen cannot be supplied at high power demand (it could only be released by decreasing the flow rate), leading to a utilisation factor, defined as the hydrogen delivered at constant power divided by the available hydrogen, which decreases as the power demand increases. Finally, it is worth noting that the upper bound defined in Section 2.2.2 is actually higher than required; this is beneficial as it lowers costs. If a higher pressure were needed, a more efficient way to satisfy the demand might be to lower the system temperature.

When hydrogen demand is high, as in Fig. 9 where the power fraction f_t ranges in the interval 0.60–1.00, controllability is limited, and the utilisation factor decreases further. Fig. 9(a) highlights that the target can only be met for a high DoH, as pressure cannot be adequately lowered to match the desired $\dot{m}_t$ (Fig. 9(b)). As long as the reactor pressure can be changed accordingly to match the demand, the DoH trend is linear. Subsequently, the performance of the uncontrolled system is followed and $\dot{m}_r$ decreases with DoH^2, as indicated by Eq. (23). In these cases, pressure still has to be raised initially with the exception of the 0.90 and 1.00 power fraction values, as a pressure drop is required even in the early stages.

3.2.2. Temperature control

Similarly to pressure control, temperature control performances are highly influenced by power demand. Again, only a demand as low as $f_t = 0.10$ (Fig. 10) leads to a full discharge ($\text{DoH}_f \leq 0.20$). An increase in the power fraction f_t results in a decrease in controllability and the utilisation factor. A final DoH of almost DoH = 0.10 is reached in Fig. 10(a) for the lowest demand, while higher values do not match the power target for the entire operating time. However, the final DoH is lower than the equivalent results in a pressure-controlled environment. A significant temperature drop ($\Delta T \geq 20$ K) is first required for the $f_t = 0.10$ and 0.20 scenarios, with a minimum temperature level of 440 K (Fig. 10(b)). Other case studies still have a temperature drop, but it is far more moderate. As such, it could be beneficial for the system to set a design operating point to lower temperature for the lowest power demand scenarios, resulting in a slight reduction in heat consumption. It must be noted that temperature T represented here is the mass-averaged temperature throughout the length of the reactor.

In contrast, high demands can only be satisfied for a limited time period (Fig. 11) and result in a higher final DoH. Fig. 11(a) shows a drop in expected performances and a final DoH as high as ≈0.47 is reached for the highest demand. Outside of the controlled regime, the mass flow rate has the typical trend of the uncontrolled system (Section 3.1). As such, a transient due to the switch between different operational modes is followed by a steady release. This alternating trend is also required by the controlled variable, whose value in Fig. 11(b) has an increasing trend throughout almost the whole operating time. Controllability is lost as the upper bound is reached.

3.2.3. Velocity control

The performance that can be achieved by controlling the flow rate through the HTF velocity (and consequently the HTF mass flow rate) is described in Figs. 12–13 for low and high power demands, respectively.

Unlike the pressure and temperature control strategies presented in Sections 3.2.1–3.2.2, in which satisfactory results are achieved for low demands, the lower bound of velocity can only prevent heat to be supplied to the reactor: in other words, in these scenarios, the HTF velocity cannot slow the reaction down enough. Therefore, the power fractions f_t in the range 0.10–0.20 are never reached, with the goal $f_t = 0.20$ only reached at the end of the simulation time (after 400 min), and with a DoH already below 0.60 (Fig. 12(a)). Therefore, their velocity profile is the same (Fig. 12(b)), since no HTF mass flow rate is required to have a temperature drop low enough that the kinetic rate slows down to the desired level. Raising f_t to 0.30 allows reaching

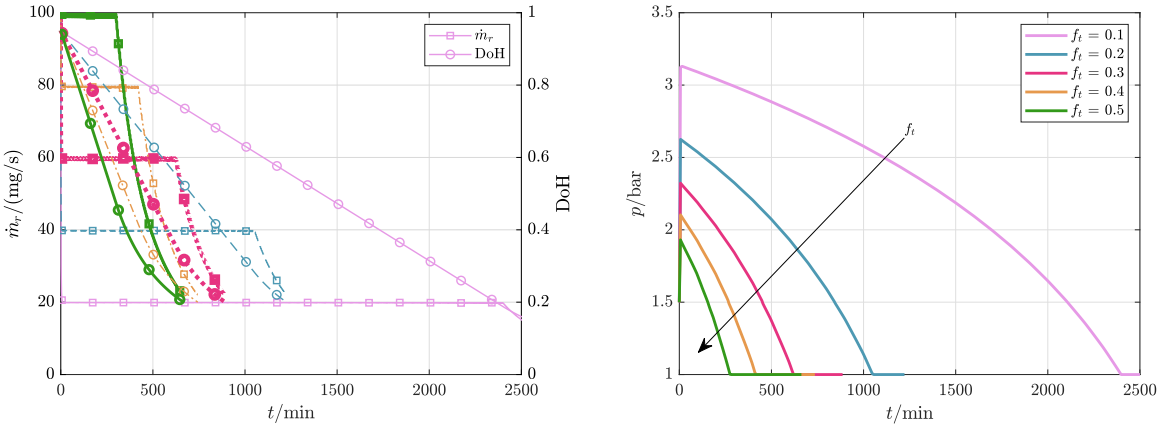

(a) Controlled hydrogen release over time. (b) Pressure trend over time.

Fig. 8. System performances with pressure control for f_t ranging from 0.10–0.50.

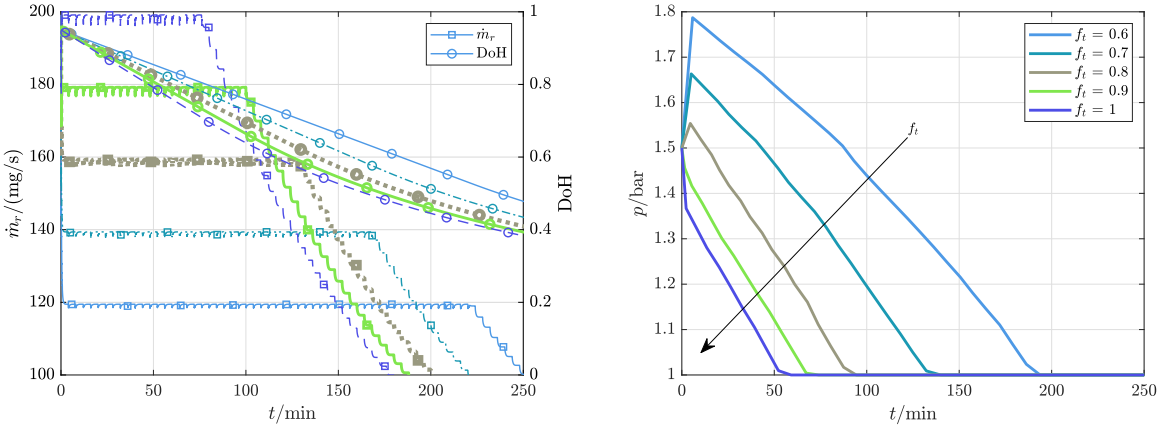

(a) Controlled hydrogen release over time. (b) Pressure trend over time.

Fig. 9. System performances with pressure control for f_t ranging from 0.60–1.00.

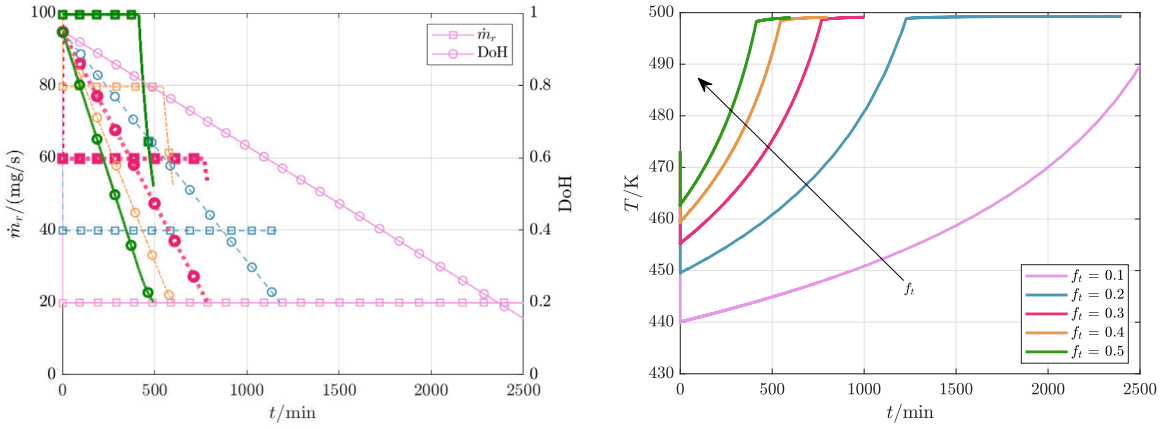

(a) Controlled hydrogen release over time. (b) Temperature trends over time.

Fig. 10. System performances with temperature control for f_t ranging from 0.10–0.50.

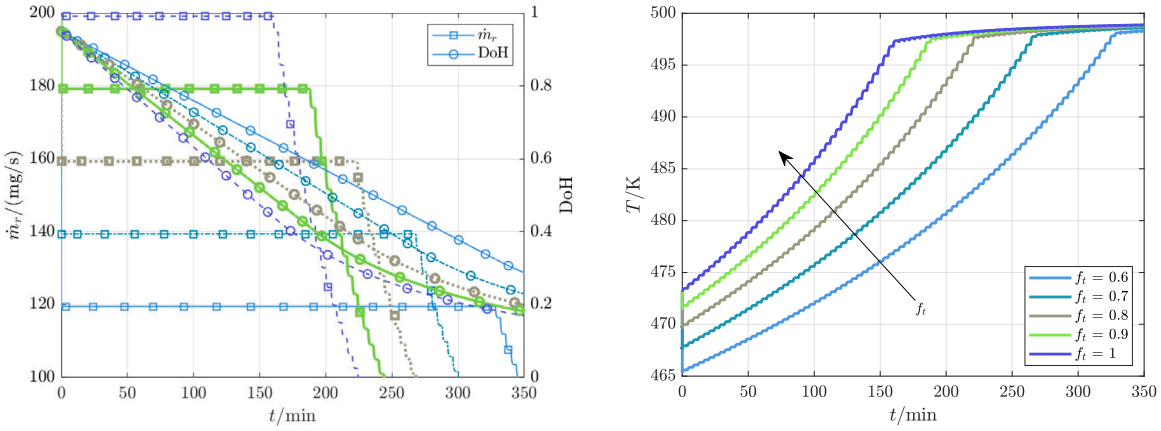

(a) Controlled hydrogen release over time. (b) Temperature trends over time.

Fig. 11. System performances with temperature control for f_t ranging from 0.60–1.00.

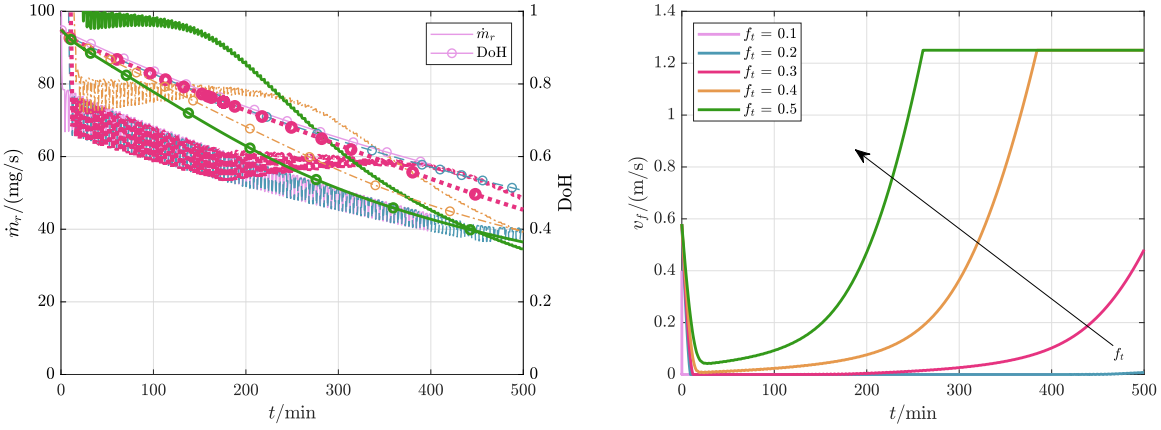

(a) Controlled hydrogen release over time. (b) HTF velocity trend over time.

Fig. 12. System performances with HTF velocity control for f_t ranging from 0.10–0.50.

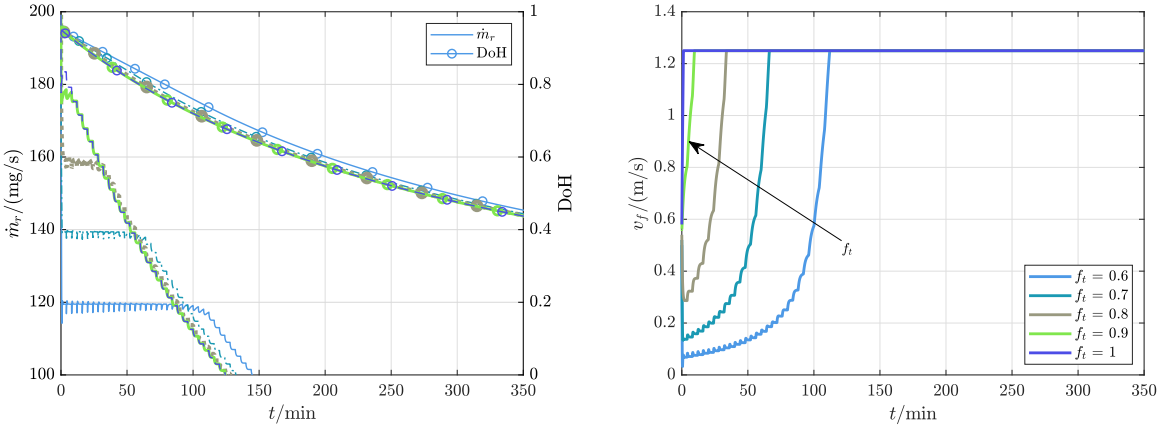

(a) Controlled hydrogen release over time. (b) HTF velocity trend over time.

Fig. 13. System performances with HTF velocity control for f_t ranging from 0.60–1.00.

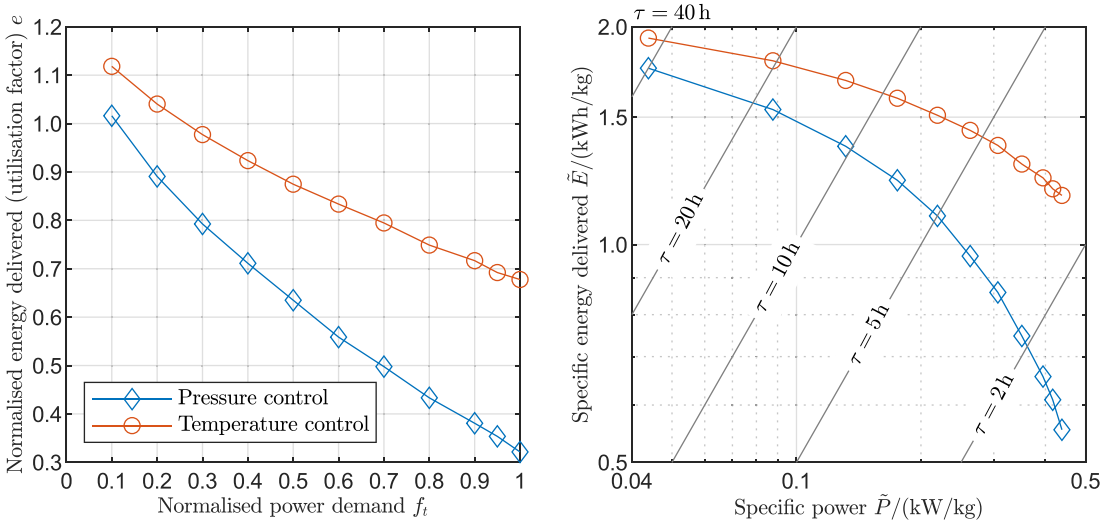

Fig. 14. Ragone diagrams of a NEC storage system under pressure and temperature control.

the target but only after about 80 min, which is a consistent time delay compared to pressure and temperature control systems. The 0.40–0.50 power fraction values are met much earlier; however, controllability is lost for still high DoH levels, even as still great controllability margins are allowed for v_f, because low demands result in low temperature drops and as such increasing the HTF heat capacity is ineffective in regulating the discharge. Because the control strategy is so ineffective, oscillations can easily be observed and would require the introduction of an intermediate hydrogen buffer to smooth them.

On the other hand, higher demands can only be met very briefly or not at all, as shown in Fig. 13(a), as $f_t = 0.60$ results in a final DoH above 0.70. As the required reaction rate is relatively high, the reaction heat rate $\dot{Q}_r$, Eq. (15), must be balanced by the heat rate $\dot{Q}_f$ provided by the HTF, Eq. (14). Thus, Fig. 13(b) shows a much tighter correlation between velocity changes and controllability time, despite a still residual possible control over v_f that does not lead to significant control enhancement over the release rate.

3.3. Ragone diagrams

The performance of the control systems acting through the reactor pressure and the HTF inlet temperature is represented in the Ragone diagrams shown in Fig. 14. In Fig. 14(a), both axes are normalised: the power demand is expressed in terms of the power fraction vaues f_t, Eq. (41), and as such can only vary between 0 and 1; the energy content, on the other hand, can be higher than unity since it is normalised through Eq. (43), where the upper threshold for the numerator is the total hydrogen content, Eq. (32), while the denominator is the available mass of hydrogen m_{H_2} in a discharge process taking into account the minimum and maximum design values of the degree of hydrogenation.

Fig. 14(b), on the other hand, shows the specific chemical energy $\tilde{E}$ delivered to the end user against the specific chemical power demand $\tilde{P}$, which are defined with reference to the total LOHC mass available in the storage system as follows:

$$\tilde{E} = m_{H_2,u}\mathrm{HHV}/m_L \tag{44}$$

$$\tilde{P} = \dot{m}_t\mathrm{HHV}/m_L \tag{45}$$

The maximum energy-to-power ratio represents the theoretical discharge duration τ_{max} of the storage system, while the actual duration τ depends on the effective amount of energy discharged, and hence it is the product of utilisation factor and theoretical discharge duration [60]:

$$\tau_{max} = \tilde{E}_{max}/\tilde{P} = m_{H_2}/\dot{m}_t \tag{46}$$

$$\tau = \tilde{E}/\tilde{P} = m_{H_2,u}/\dot{m}_t = e\tau_{max} \tag{47}$$

The Ragone diagram representing specific quantities (Fig. 14(b)) allows the identification of an effective range of discharge duration resulting in utilisation factors above 80 %: in the case of the control system relying on HTF temperature, this range is approximately 5–40 h, while for pressure control it is around 10–40 h. However, it is important to recall that the ratio f_r of the LOHC mass within the reactor and the total stored LOHC mass, Eq. (33), directly affects these values and, in particular, the specific power: since only the mass within the reactor, equal to $f_r m_L$, contributes to the reaction, an increase in f_r obviously leads to a corresponding increase in specific power and a decrease in discharge duration. For example, doubling the ratio f_r halves the value of τ corresponding to the same utilisation factor, meaning that the system is more suitable for relatively high power demands compared to the energy stored. In other words, the highest specific power and the fastest discharge duration are obtained with $f_r = 1$, representing a storage system without vessels and the entire LOHC mass directly contained in the reactor: in that case, the specific power and discharge duration would be five times higher and lower, respectively, than in the case analysed in this paper, as found in a previous paper by the authors, where a simplified reactor and only pressure control was considered [60].

As discussed in Section 3.2, low values of power requirements allow for a deep discharge: this is beneficial in terms of compactness and energy density. As normalised power demand increases, the amount of hydrogen that can be effectively discharged decreases, leading to a reduction in the utilisation factor. This effect can be seen as a reduction in the energy density of the system, since the desired mass flow rate can only be provided for high values of DoH, and at lower values the system is unable to feed the end-user. Temperature control has better performances: controllability is both higher and more consistent. However, to reach a utilisation factor of at least 80 % of the standard storage capacity, the normalised power demand f_t must be lower than 70 % and 30 % for temperature and pressure control, respectively.

In the case of a load that changes with time, these graphs have to be read as follows. Given a control strategy (e.g. pressure) and a normalised power demand with a given maximum (e.g. $f_{t,max} = 0.6$), the system can follow the dynamic load completely only until the normalised energy delivered level falls to the level corresponding the maximum power demand (in this case, $e \approx 0.55$ corresponding to $f_{t,max} = 0.6$ in Fig. 14(a)). Afterwards, lower loads can still be met effectively, while at higher loads the system is beyond controllability: the lower pressure bound has been met, so no further control is achievable,

and the hydrogen release follows the uncontrolled system unloading associated to that pressure and temperature level, until the load falls back to suitably low values, compatible with the current storage level.

4. Conclusions

This paper presents a newly introduced plug flow reactor design coupled with two vessels to allow for discontinuous operation and reduced length. Such reactor is put in a LOHC-based storage system subjected to three alternative control strategies, and coupled with increasingly higher power demands.

Different control systems have been tested to control the mass flow rate of hydrogen released by the reactor, simulating different levels of constant power demand required by an end user. Control systems act separately on either the reactor pressure, the HTF inlet temperature, or the HTF inlet velocity. The controllability of the system is assessed by means of the effective operating time during which the reactor can supply the required flow rate, which allows the definition of a utilisation factor. Both temperature and pressure control systems demonstrate great controllability with low power demand. Although the performance of the pressure control decreases rapidly as demand increases, the temperature control is more consistent. However, a power demand greater than 70 % the reference value would lead to unsatisfactory values of the utilisation factor. These results are used to plot Ragone diagrams to highlight these performances; moreover, the results show that these hydrogen storage systems can be effectively used in applications with discharge durations approximately in the range 5–40 h if the mass of LOHC within the reactor is 20 % of the total mass of LOHC stored in the system.

On the other hand, the heat transfer fluid mass flow rate is inadequate to lead reaction rate control and should only be used coupled with other controlled variables.

This paper aims to share an innovative view of LOHC systems, focusing on controllability margins, comparing controlled variable alternatives, and providing a sizing guide when coupling a LOHC system with end-user demand.

Nomenclature

A_{hex}	m^2	heat exchange surface
b	1/bar	pressure coefficient
c	kJ/(kg K)	specific heat capacity
c_1	–	binary turn-based coefficient [1: during odd turns, 0: during even turns]
c_2	–	binary turn-based coefficient [1: during even turns, 0: during odd turns]
D	m	diameter
d_p	m	catalyst particle diameter
e	–	dimensionless (normalised) energy
E	kJ	energy
E_a	kJ/mol_{H_2}	activation energy
$\dot{E}_m$	kW	total energy flow rate
f	–	friction factor
f_r	–	reactor mass ratio
f_t	–	target factor
f_x		mass flow rate ratio
H_r	kJ/kg	reaction enthalpy
h	kJ/kg	specific enthalpy
j_{turn}	–	turn number
k_0	min	frequency factor
m	kg	mass
N	–	number of grid elements
P	kW	power
p	bar	pressure
$\dot{Q}$	kW	rate of heat transfer
R_u	8.3145 kJ/(kmol K)	universal gas constant
T	K	temperature
t	s	time
t_v	s	vessel discharge time
u	kJ/kg	specific internal energy
v	m/s	velocity
U	$kW/(K\,m^2)$	overall heat transfer coefficient
$w_{\%}$	–	gravimetric storage capacity
Greek letters		
α	$kW/(K\,m^2)$	convective heat transfer coefficient
Δp_{loss}	Pa	pressure drop
ϵ	–	heat transfer effectiveness
ϵ_{tube}	m	tube roughness
η	–	efficiency
λ	kW/(K m)	thermal conductivity
ρ	kg/m^3	density
τ	s	discharge duration
Ω	m^2	cross section
Subscripts		
0		initial
1		heat exchanger inner wall
2		heat exchanger outer wall
des		design
f		heat transfer fluid
hyd		hydraulic
i		generic element index
$\bar{i}$		last reactor element index in a given turn
in		inlet flow rate
L		liquid organic hydrogen carrier
max		maximum
min		minimum
out		outlet flow rate
$pump$		pumping
r		reaction-related
t		target
u		end user
v, a		active vessel
v, p		passive vessel
Acronyms		
DoH		Degree of Hydrogenation
HHV		Higher Heating Value
HTF		Heat Transfer Fluid
LOHC		Liquid Organic Hydrogen Carrier
NEC		N-Ethyl-Carbazole
Nu		Nusselt number
PFR		Plug Flow Reactor
Pr		Prandtl number
Re		Reynolds number

CRediT authorship contribution statement

Marco Gambini: Validation, Visualization. **Federica Guarnaccia:** Conceptualization, Methodology, Software, Validation, Writing – original draft, Writing – review & editing, Visualization. **Michele Manno:** Conceptualization, Methodology, Validation, Writing – review & editing, Visualization, Supervision. **Michela Vellini:** Validation, Visualization.

Declaration of competing interest

The authors declare that they have no known competing financial interests or personal relationships that could have appeared to influence the work reported in this paper.

References

[1] Liu W, Zuo H, Wang J, Xue Q, Ren B, Yang F. The production and application of hydrogen in steel industry. Int J Hydrogen Energy 2021;46(17):10548–69. http://dx.doi.org/10.1016/j.ijhydene.2020.12.123.

[2] Röben FT, Schöne N, Bau U, Reuter MA, Dahmen M, Bardow A. Decarbonizing copper production by power-to-hydrogen: A techno-economic analysis. J Clean Prod 2021;306:127191. http://dx.doi.org/10.1016/j.jclepro.2021.127191.

[3] David P. Update on hydrogen injection in cement plants. 2022, https://www.globalcement.com/news/item/14637-update-on-hydrogen-injection-in-cement-plants. [Accessed 20 September 2023].

[4] IEA. Energy system: Low-emission fuels: Hydrogen. 2023, https://www.iea.org/energy-system/low-emission-fuels/hydrogen. [Accessed 10 September 2023].

[5] Bent Erik B, Frida B, Theo B, Hendrik B, Ida SB, Kaveh D, et al. Hydrogen forecast to 2050. Technical report, DNV; 2022.

[6] Herib B, Emanuele B, Barbara J, Jeffrey L, Noam B, Melissa S, et al. Enabling measures roadmap for green hydrogen. Technical report, IRENA; 2022.

[7] Hydrogen Council. Path to hydrogen competitiveness: A cost perspective. 2020.

[8] Mazloomi K, Gomes C. Hydrogen as an energy carrier: Prospects and challenges. Renew Sustain Energy Rev 2012;16(5):3024–33. http://dx.doi.org/10.1016/j.rser.2012.02.028.

[9] Meiling Y, Hugo L, Elodie P, Robin R, Samir J, Daniel H. Hydrogen energy systems: A critical review of technologies, applications, trends and challenges. Renew Sustain Energy Rev 2021;146. http://dx.doi.org/10.1016/j.rser.2021.111180.

[10] Dutta S. A review on production, storage of hydrogen and its utilization as an energy resource. J Ind Eng Chem 2014;20(4):1148–56. http://dx.doi.org/10.1016/j.jiec.2013.07.037.

[11] Dincer I, Acar C. Review and evaluation of hydrogen production methods for better sustainability. Int J Hydrogen Energy 2015;40(34):11094–111. http://dx.doi.org/10.1016/j.ijhydene.2014.12.035.

[12] Chaubey R, Sahu S, James OO, Maity S. A review on development of industrial processes and emerging techniques for production of hydrogen from renewable and sustainable sources. Renew Sustain Energy Rev 2013;23:443–62. http://dx.doi.org/10.1016/j.rser.2013.02.019.

[13] Parra D, Valverde L, Pino FJ, Patel MK. A review on the role, cost and value of hydrogen energy systems for deep decarbonisation. Renew Sustain Energy Rev 2019;101:279–94. http://dx.doi.org/10.1016/j.rser.2018.11.010.

[14] Dagdougui H, Sacile R, Bersani C, Ouammi A. Chapter 4 - Hydrogen Storage and Distribution: Implementation Scenarios. In: Dagdougui H, Sacile R, Bersani C, Ouammi A, editors. Hydrogen Infrastructure for Energy Applications. Academic Press; 2018, p. 37–52. http://dx.doi.org/10.1016/B978-0-12-812036-1.00004-4.

[15] Bellocchi S, Colbertaldo P, Manno M, Nastasi B. Assessing the effectiveness of hydrogen pathways: A techno-economic optimisation within an integrated energy system. Energy 2023;263:126017. http://dx.doi.org/10.1016/j.energy.2022.126017.

[16] Bellocchi S, Manno M, Noussan M, Vellini M. Impact of grid-scale electricity storage and electric vehicles on renewable energy penetration: A case study for Italy. Energies 2019;12(7):1303. http://dx.doi.org/10.3390/en12071303.

[17] Abe J, Popoola A, Ajenifuja E, Popoola O. Hydrogen energy, economy and storage: Review and recommendation. Int J Hydrogen Energy 2019;44(29):15072–86. http://dx.doi.org/10.1016/j.ijhydene.2019.04.068.

[18] Moradi R, Groth KM. Hydrogen storage and delivery: Review of the state of the art technologies and risk and reliability analysis. Int J Hydrogen Energy 2019;44(23):12254–69. http://dx.doi.org/10.1016/j.ijhydene.2019.03.041.

[19] Tang D, Tan G-L, Li G-W, Liang J-G, Ahmad SM, Bahadur A, et al. State-of-the-art hydrogen generation techniques and storage methods: A critical review. J Energy Storage 2023;64:107196. http://dx.doi.org/10.1016/j.est.2023.107196.

[20] Hirscher M, Yartys VA, Baricco M, von Colbe JB, Blanchard D, Bowman RC, et al. Materials for hydrogen-based energy storage – past, recent progress and future outlook. J Alloys Compd 2020;827:153548. http://dx.doi.org/10.1016/j.jallcom.2019.153548.

[21] US Department of Energy. Energy requirements for hydrogen gas compression and liquefaction as related to vehicle storage needs. In: DOE hydrogen and fuel cells program record. 2009, https://www.hydrogen.energy.gov/pdfs/9013_energy_requirements_for_hydrogen_gas_compression.pdf. [Accessed 25 October 2022].

[22] Al Ghafri SZ, Munro S, Cardella U, Funke T, Notardonato W, Trusler JPM, et al. Hydrogen liquefaction: a review of the fundamental physics, engineering practice and future opportunities. Energy Environ Sci 2022;15:2690–731. http://dx.doi.org/10.1039/D2EE00099G.

[23] He T, Pei Q, Chen P. Liquid organic hydrogen carriers. J Energy Chem 2015;24(5):587–94. http://dx.doi.org/10.1016/j.jechem.2015.08.007.

[24] Muthukumar P, Kumar A, Afzal M, Bhogilla S, Sharma P, Parida A, et al. Review on large-scale hydrogen storage systems for better sustainability. Int J Hydrogen Energy 2023. http://dx.doi.org/10.1016/j.ijhydene.2023.04.304.

[25] Geiling, Wagner, Auer, Ortner, Nuß, Seyfried, et al. Operational experience with a liquid organic hydrogen carrier (LOHC) system for bidirectional storage of electrical energy over 725 h. J Energy Storage 2023. http://dx.doi.org/10.1016/j.est.2023.108478.

[26] Dennis J, Bexten T, Petersen N, Wirsum M, Preuster P. Model-based analysis of a liquid organic hydrogen carrier (LOHC) system for the operation of a hydrogen-fired gas turbine. J Eng Gas Turbines Power 2021;143(3):031011. http://dx.doi.org/10.1115/1.4048596.

[27] Rong Y, Chen S, Li C, Chen X, Xie L, Chen J, et al. Techno-economic analysis of hydrogen storage and transportation from hydrogen plant to terminal refueling station. Int J Hydrogen Energy 2023. http://dx.doi.org/10.1016/j.ijhydene.2023.01.187.

[28] Correa G, Volpe F, Marocco P, Muñoz P, Falagüerra T, Santarelli M. Evaluation of levelized cost of hydrogen produced by wind electrolysis: Argentine and Italian production scenarios. J Energy Storage 2022;52:105014. http://dx.doi.org/10.1016/j.est.2022.105014.

[29] Muragishi O, Inatsu S, Uraguchi R, Yamashiro K, Imai T, Ohashi T, et al. Hydrogen transportation — Development of liquefied hydrogen carrier. 2021, https://global.kawasaki.com/en/corp/rd/magazine/182/pdf/n182en07.pdf.

[30] Gambini M, Guarnaccia F, Di Vona ML, Manno M, Vellini M. Liquid organic hydrogen carriers: Development of a thermodynamic and kinetic model for the assessment of hydrogenation and dehydrogenation processes. Int J Hydrogen Energy 2022;47(65):28034–45. http://dx.doi.org/10.1016/j.ijhydene.2022.06.120.

[31] Díaz E, Rapado-Gallego P, Ordóñez S. Systematic evaluation of physicochemical properties for the selection of alternative liquid organic hydrogen carriers. J Energy Storage 2023;59:106511. http://dx.doi.org/10.1016/j.est.2022.106511.

[32] Niermann M, Beckendorff A, Kaltschmitt M, Bonhoff K. Liquid Organic Hydrogen Carrier (LOHC) – Assessment based on chemical and economic properties. Int J Hydrogen Energy 2019;44(13):6631–54. http://dx.doi.org/10.1016/j.ijhydene.2019.01.199.

[33] Li L, Aravind PV, Woudstra T, van den Broek M. Assessing the waste heat recovery potential of liquid organic hydrogen carrier chains. Energy Convers Manage 2022. http://dx.doi.org/10.1016/j.enconman.2022.116555.

[34] Müller K, Thiele S, Wasserscheid P. Evaluations of concepts for the integration of fuel cells in liquid organic hydrogen carrier systems. Energy Fuels 2019. http://dx.doi.org/10.1021/acs.energyfuels.9b01939.

[35] Haupt A, Müller K. Integration of a LOHC storage into a heat-controlled CHP system. Energy 2016. http://dx.doi.org/10.1016/j.energy.2016.10.129.

[36] Spatolisano E, Restelli F, Matichecchia A, Pellegrini LA, de Angelis AR, Cattaneo S, et al. Assessing opportunities and weaknesses of green hydrogen transport via LOHC through a detailed techno-economic analysis. Int J Hydrogen Energy 2023. http://dx.doi.org/10.1016/j.ijhydene.2023.08.040.

[37] Sotoodeh F, Huber BJ, Smith KJ. The effect of the N atom on the dehydrogenation of heterocycles used for hydrogen storage. Appl Catal A: General 2012;419–420:67–72.

[38] Gambini M, Guarnaccia F, Manno M, Vellini M. Thermal design and heat transfer optimisation of a Liquid Organic Hydrogen Carrier batch reactor for hydrogen storage. Int J Hydrogen Energy 2023;48:37625–36. http://dx.doi.org/10.1016/j.ijhydene.2023.08.200.

[39] Gambini M, Guarnaccia F, Manno M, Vellini M. Hydrogen flow rate control in a liquid organic hydrogen carrier batch reactor for hydrogen storage. Int J Hydrogen Energy 2023. http://dx.doi.org/10.1016/j.ijhydene.2023.05.153.

[40] Bourane A, Elanany M, Pham TV, Katikaneni SP. An overview of organic liquid phase hydrogen carriers. Int J Hydrogen Energy 2016;41(48):23075–91. http://dx.doi.org/10.1016/j.ijhydene.2016.07.167.

[41] House JE. Principles of chemical kinetics. Academic Press; 2007.

[42] Peters R, Deja R, Fang Q, Nguyen VN, Preuster P, Blum L, et al. A solid oxide fuel cell operating on liquid organic hydrogen carrier-based hydrogen – A kinetic model of the hydrogen release unit and system performance. Int J Hydrogen Energy 2019;44(26):13794–806. http://dx.doi.org/10.1016/j.ijhydene.2019.03.220.

[43] Cho J-H, Yu S-S, Kim M-Y, Kang S-G, Lee Y-D, Ahn K-Y, et al. Dynamic modeling and simulation of hydrogen supply capacity from a metal hydride tank. Int J Hydrogen Energy 2013. http://dx.doi.org/10.1016/j.ijhydene.2013.02.142.

[44] Aruna R, Christa SJ. Modeling, system identification and design of fuzzy PID controller for discharge dynamics of metal hydride hydrogen storage bed. Int J Hydrogen Energy 2019. http://dx.doi.org/10.1016/j.ijhydene.2019.11.238.

[45] Krane P, Nash AL, Ziviani D, Braun JE, Marconnet AM, Jain N. Dynamic modeling and control of a two-reactor metal hydride energy storage system. Appl Energy 2022;325:119836. http://dx.doi.org/10.1016/j.apenergy.2022.119836.

[46] Geiling J, Steinberger M, Ortner F, Seyfried R, Nuß A, Uhrig F, et al. Combined dynamic operation of PEM fuel cell and continuous dehydrogenation of perhydrodibenzyltoluene. Int J Hydrogen Energy 2021;46(72):35662–77. http://dx.doi.org/10.1016/j.ijhydene.2021.08.034.

[47] Fikrt A, Brehmer R, Milella V-O, Müller K, Bösmann A, Preuster P, et al. Dynamic power supply by hydrogen bound to a liquid organic hydrogen carrier. Appl Energy 2017;194:1–8. http://dx.doi.org/10.1016/j.apenergy.2017.02.070.

[48] Yang Y, Yao J, Wang H, Yang F, Wu Z, Zhang Z. Study on high hydrogen yield for large-scale hydrogen fuel storage and transportation based on liquid organic hydrogen carrier reactor. Fuel 2022;321:124095. http://dx.doi.org/10.1016/j.fuel.2022.124095.

[49] Rao N, Lele AK, Patwardhan AW. Optimization of Liquid Organic Hydrogen Carrier (LOHC) dehydrogenation system. Int J Hydrogen Energy 2022;47(66):28530–47. http://dx.doi.org/10.1016/j.ijhydene.2022.06.197.

[50] Bollmann J, Schmidt N, Beck D, Preuster P, Zigan L, Wasserscheid P, et al. A path to a dynamic hydrogen storage system using a liquid organic hydrogen carrier (LOHC): Burner-based direct heating of the dehydrogenation unit. Int J Hydrogen Energy 2023;48(3):1011–23. http://dx.doi.org/10.1016/j.ijhydene.2022.09.234.

[51] Ragone DV. Review of battery systems for electrically powered vehicles. SAE Techn Pap 1968;680453. http://dx.doi.org/10.4271/680453.

[52] Christen T, Carlen MW. Theory of Ragone plots. J Power Sources 2000;91(2):210–6. http://dx.doi.org/10.1016/S0378-7753(00)00474-2.

[53] Christen T. Ragone plots and discharge efficiency-power relations of electric and thermal energy storage devices. J Energy Storage 2020;27:101084. http://dx.doi.org/10.1016/j.est.2019.101084.

[54] Perry RH, Green DW, Southard MZ. Perry's chemical engineers' handbook. McGraw-Hill Education; 2022.

[55] Bell IH, Wronski J, Quoilin S, Lemort V. Pure and pseudo-pure fluid thermophysical property evaluation and the open-source thermophysical property library CoolProp. Ind Eng Chem Res 2014;53(6):2498–508. http://dx.doi.org/10.1021/ie4033999, URL http://pubs.acs.org/doi/abs/10.1021/ie4033999.

[56] Caroline W, Christina W, Stephanie S, Florian L, Moritz H, Josef K, et al. Pressurized solid oxide fuel cells: Operational behavior. 2011, https://core.ac.uk/reader/11147430.

[57] Wang B, Chang T-y, Jiang Z, Wei J-j, Zhang Y-h, Yang S, et al. Catalytic dehydrogenation study of dodecahydro-n-ethylcarbazole by noble metal supported on reduced graphene oxide. Int J Hydrogen Energy 2018;43(15):7317–25. http://dx.doi.org/10.1016/j.ijhydene.2018.02.156.

[58] Xie L-J, Jiang J-C, Huang A-C, 1 YT, Liu Y-C, Zhou H-L, et al. Calorimetric evaluation of thermal stability of organic liquid hydrogen storage materials and metal oxide additives. Energies 2022;15:2236. http://dx.doi.org/10.3390/en15062236.

[59] Stark K, Keil P, Schug S, Müller K, Wasserscheid P, Arlt W. Melting points of potential liquid organic hydrogen carrier systems consisting of N-alkylcarbazoles. J Chem Eng Data 2016;61:1441–8. http://dx.doi.org/10.1021/acs.jced.5b00679.

[60] Gambini M, Guarnaccia F, Manno M, Vellini M. Ragone plots of material-based hydrogen storage systems. J Energy Storage 2023;76:109815. http://dx.doi.org/10.1016/j.est.2023.109815.